Development, characterization and modeling of new concepts in the design of honeycombs used in composite panels

André de Jesus Valado Miranda
andre.j.v.miranda@tecnico.ulisboa.pt

Instituto Superior Técnico, Universidade de Lisboa, Portugal
November 2019

Abstract

The present work aims to evaluate the flexural properties of honeycomb structures with new configurations and orientations in the plane, produced by additive and subtractive manufacturing processes. Indeed, structures with regular hexagonal (Hr), Lotus (Lt) and hexagonal with Plateau borders (Pt) configurations, with 0°, 45°, and 90° orientations were analyzed. To evaluate the properties of these honeycombs, 3-point bending tests were performed on the structures, both experimentally and by numerical modeling. In the latter, the finite element method was used, with honeycombs of two aluminum alloys and polylactic acid (PLA). The structures produced in aluminum were obtained by Selective Laser Melting (SLM) technology and machining, while PLA structures were obtained by Fused Deposition Modeling (FDM). From the stress distribution analysis and the force-displacement curves, it was possible to determine the strength, stiffness, and energy absorbed by the structures. Failure modes were also analyzed for PLA honeycombs, both numerically and experimentally. In general, a strong correlation was observed between numerical and experimental results. The results show that the stiffness and absorbed energy evolve increasingly in the order, Hr, Pt, Lt, and with the orientation through the sequence, 45°, 90°, 0°. Thus, Lt structures with 0° orientation are alternatives to the traditional honeycombs used in sandwich composite panels for aerospace applications where low weight, high stiffness, and excellent energy-absorbing capacity are required.

Key-words
Honeycomb, Mechanical properties, Finite Element Analysis, Selective Laser Melting, Fused Deposition Modeling

1. Introduction

The aerospace, automotive and marine industries are heavily reliant on sandwich panels with cellular material cores, due to their low weight, high stiffness-to-weight ratio, high strength-to-weight ratio, excellent capability for absorbing energy and good thermal insulation properties. Aluminum honeycombs with hexagonal cells are the most commonly used as core [1]–[7]. The economic and environmental benefits of the increase use of sandwich panels in transport means reduced weight of structures and consequently greater efficiency and sustainability of vehicles [3], [7]. The design of alternative lightweight structures is not simple due to its potential geometric complexity. However, recent progresses in additive manufacturing technologies have enabled an easier production of such structures, due to its inherent greater flexibility in manufacturing [7]. Additive manufacturing encompasses a variety of technologies that create three-dimensional (3D) objects, layer by layer, through the total or partial fusion of a material [7]–[9]. In this work, the Selective Laser Melting (SLM) and Fused Deposition Modeling (FDM) processes were used. The SLM process consists of the complete fusion of metal powders in inert gas print chambers. The final parts obtained can have relative densities of up to 99.9% [7]–[10]. The FDM process uses the heating of thermoplastic polymers that are extruded by a print nozzle to form each layer. The parts produced by this process have a substructure called infill inside, and externally (along the contour) they are formed by shell substructures. Shells have greater stiffness and strength than infill and a higher strength infill is achieved with a higher infill density [7], [11], [12].

The response of honeycomb cores to shearing is of great importance, as sandwich panels are often subject to bending [3], [5], [6].

To our best knowledge, there is little research on honeycombs with innovative geometries produced by additive manufacturing, thus this

work intends to provide a contribution to this field. In this investigation, a comparative study of the mechanical properties of three types of configurations and orientations was carried out. Finite element simulations of bending tests were performed to the designed structures. The FE results were validated by testing metallic and polymeric samples. The FE and experimental results have good agreement.

2. Materials and methods

The honeycomb structures were designed using SOLIDWORKS 2018 software, with regular hexagonal (Hr), Lotus (Lt) and hexagonal with Plateau borders (Pt) configurations, and 0°, 45° and 90° orientations. The models will be named by the configuration type followed by the orientation in degrees. For example, a structure with Lotus configuration and orientation 45° is called Lt_45. Schemes of the studied configurations and the respective geometrical parameters are presented in figure 1. Figure 2 shows how to obtain the different orientations for Lt models, from to the geometric pattern of the respective configuration.
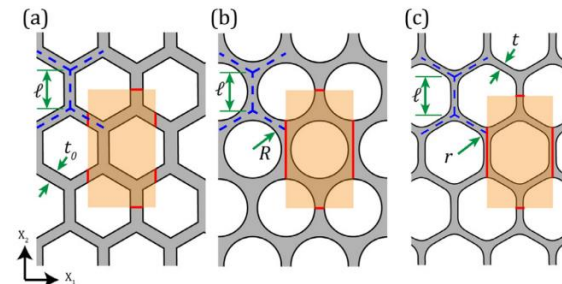
Figure 1: Configurations and geometric parameters of the structures designed [13].
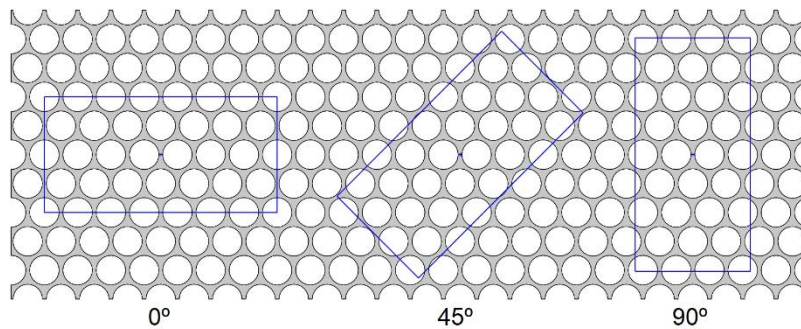
Figure 2: Example of obtaining different orientations for a Lt configuration.

An important parameter when analyzing cellular materials is the relative density, $\bar{\rho}$, which is defined as the ratio between the density of cellular material and the density of solid material constituting its walls. The structures were designed to have a relative density in the range 0.22 to 0.29, with $l = 11.26$mm, $t_0 = t = 2.31$mm, $R = 8.66$mm, and $r = 4.504$mm.

Three materials were used in the production of the structures, namely a cast aluminum alloy according to DIN EN 1706:2013, called aluminum-A, a 7075 T6 aluminum alloy, called aluminum-S, and the PLA polymer.

Models created for each material have the same number of cells. Aluminum-S and PLA honeycombs have dimensions around 136.52 × 67.56 × 10mm, while aluminum-A honeycombs, by manufacturing reasons, have around 117.02 × 67.56 × 10mm. Aluminum-A honeycombs due to size reduction are designated by an asterisk following the nomenclature adopted above (for example, Hr_0*).

The aluminum-A structures were produced using SLM technology on an SLM Solutions 125HL device. The aluminum-S structures were machined on a 3-axis CNC vertical milling machine, model VF-2SS from Haas Automation, Inc. PLA structures were produced using the FDM process on an Ultimaker 3 printer. The Cura software was used to set printing parameters, namely a layer thickness of 0.1mm, an extrusion temperature of 210°C, a build plate temperature of 60°C, a print speed of 80mm/s and an infill density equal to 100%.

To determine the mechanical properties of the PLA after printing, specimens with the geometry and dimensions shown in figure 3 were designed according to ASTM E466-07 (Standard Practice for Conducting Force Controlled Constant Amplitude Axial Fatigue Tests of Metallic Materials).
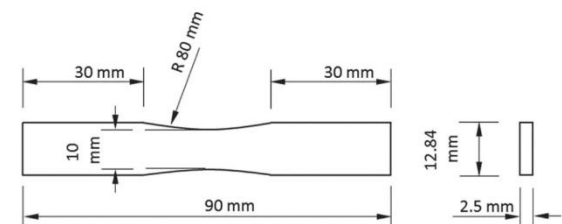
Figure 3: PLA specimen geometry and dimensions [14].

The parameter that varied was the raster angle, α, which took the values 0°/90° and 45°/-45°,

keeping the other printing parameters mentioned above unchanged. Tensile tests following ASTM D638-14 (Standard Test Method for Tensile Properties of Plastics) were performed on the specimens on an Instron 3369 universal testing machine with a 50kN load cell. Through the Bluehill software, the values of force and displacement were obtained, which served to determine Young's modulus E, yield strength σ_Y, ultimate strength σ_U, and ultimate strain ϵ_U, for each value of α.

Table 1 shows the physical and mechanical properties of the two types of aluminum used according to the information provided by the manufacturers, as well as the PLA properties for each value of α.

2.1. Finite element method simulations

Finite element models were developed using ABAQUS software, version 6.19. The supports of the 3-point bending tests were modeled as a discrete rigid material, having a radius of 5mm. Honeycombs were modeled as elastic-plastic, with linear and isotropic hardening. The materials used have a density ρ, Young's modulus E, Poisson's ratio ν, yield strength σ_Y, ultimate strength σ_U, and ultimate strain ϵ_U, as mentioned in table 1. For PLA honeycombs with 0° and 90° orientation, the properties obtained for $\alpha = 0°/90°$ were used, and for 45° orientation honeycombs, the properties for $\alpha = 45°/-45°$. The distance between lower supports was taken equal to 80mm. Contact was considered with a tangential behavior and friction coefficient of 0.20. Concerning the boundary conditions used, the lower supports have all degrees of freedom fixed and the upper support has a displacement of 2.5mm in the simulations of aluminum honeycombs and 8mm for PLA honeycombs. For honeycombs with 0° and 90° orientations, the symmetry boundary condition according to X (option XSYMM) was also used. The mesh of the supports and honeycombs were made automatically by defining the approximate global size. The support meshes have R3D4 (a 4-node 3D bilinear rigid quadrilateral) and R3D3 (a 3-node 3D rigid triangular facet) elements, whereas honeycomb meshes have only C3D8R (an 8-node linear brick, reduced integration, hourglass control) elements.

Table 1: Physical and mechanical properties of the aluminum-A [15], aluminum-S [16], and PLA [17].

Materials	ρ (g/cm³)	E (GPa)	ν	σ_Y (MPa)	σ_U (MPa)	ϵ_U
Aluminum-A	2.68	59 ± 21	0.33	211	375	0.08
Aluminum-S	2.80	71.7	0.33	503	572	0.11
PLA ($\alpha = 0°/90°$)	1.252	1.2692	0.36	25.2	48.7	0.048
PLA ($\alpha = 45°/-45°$)	1.252	1.2337	0.36	25.3	52.6	0.055

A von Mises stress convergence analysis was performed on the Hr_0, Lt_0, and Pt_0 models in the elastic regime and using $E = 1.3$GPa and $\nu = 0.36$. Note that due to symmetry only half of the honeycombs were simulated in this analysis. The point chosen for analysis has the same coordinates in all models and is in the plane of symmetry used at the bottom of the honeycombs so as not to be in the contact zone. Although convergence should be formally analyzed for all models and orientations, in this paper it was assumed that the results obtained also apply to the remaining orientations, since convergence is mainly related to the type and size of element, as not as much of microstructure. To maintain a similar number of elements, for models with Hr and Pt configuration an approximate global size of 0.6 mm was used and for the Lt configuration an approximate global size of 0.7mm.

After the simulations it was possible to determine the force exerted by the upper support on the honeycombs as a function of the displacement of this support, obtaining numerical force-displacement curves. The initial stiffness K (slope of the linear region of the curves) and the energy absorbed by the honeycombs, E_a, until maximum considered load were evaluated. From the von Mises stress distribution, it was possible to evaluate the maximum stress, a measure of the strength of simulated models.
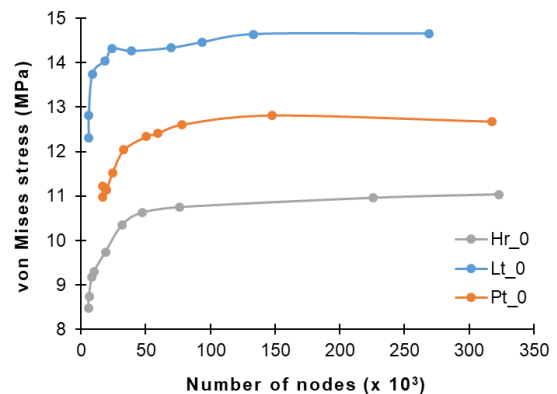
Figure 4: Evolution of von Mises stress in simulated honeycombs as a function of their number of nodes.

3

2.2. Experimental tests

The 3-point bending (3PB) tests were performed according to ASTM D790-17 (Standard Test Methods for Flexural Properties of Unreinforced and Reinforced Plastics and Electrical Insulating Materials) on an Instron 3369 universal testing machine with a 50kN load cell. A cross-head speed of 0.5mm/min was used for aluminum models, while a speed of 2.5mm/min was used for PLA models. In the tests of aluminum-A models, the final displacement of the upper support (Δ) was 1mm, while for aluminum-S models it was 1.5mm. For PLA models the tests were performed until the honeycombs fractured.

Bluehill data acquisition software was used to obtain the experimental force-displacement curves, from which stiffness, K, and energy, E_a, were determined. The failure modes of PLA models were further experimentally evaluated.

3. Results and discussion

For aluminum-A honeycombs, figure 5 shows the force-displacement curves obtained in the simulations (for the different E values) as well as the experimental ones. Table 2 presents the numerical and experimental results of K and E_a of these honeycombs and the maximum von Mises stress, $\bar{\sigma}_{max}$. All parameters were normalized to relative density.
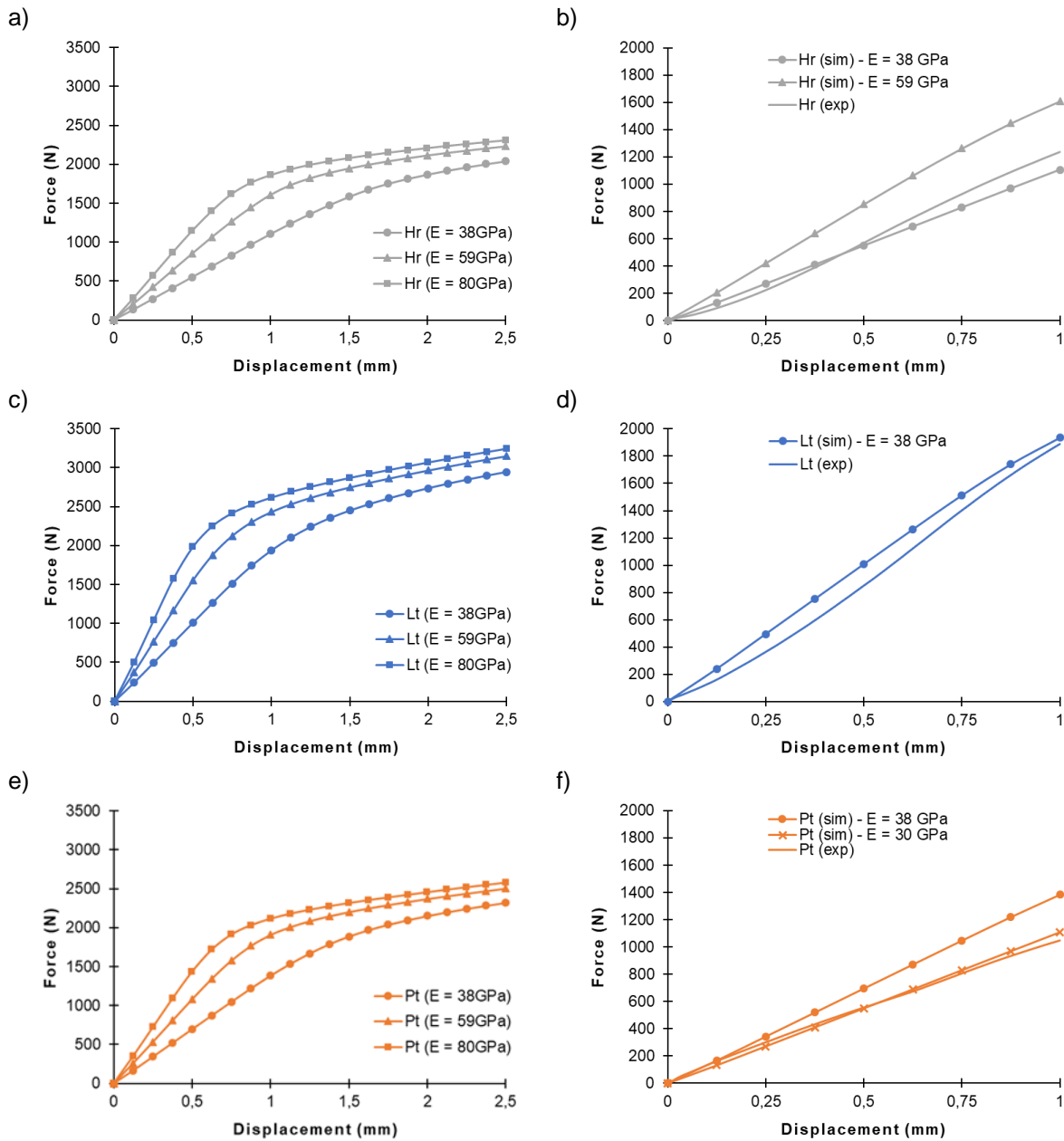
Figure 5: Force-displacement curves for aluminum-A honeycombs. (a), (c), (e) Numerical curves up to Δ = 2.5mm. (b), (d), (f) Numerical-experimental comparison up to Δ = 1mm. Configuration: (a) - (b) Hr, (c) - (d) Lt, (e) - (f) Pt.

Table 2: Numerical-experimental properties of aluminum-A honeycombs for E = 38GPa and Δ = 1mm.

Model	$\bar{\rho}$	Finite elements			Experimental	
		$\bar{\sigma}_{max}/\bar{\rho}$ (MPa)	$K/\bar{\rho}$ (N/mm)	$E_a/\bar{\rho}$ (J)	$K/\bar{\rho}$ (N/mm)	$E_a/\bar{\rho}$ (J)
Hr_0*	0,223	$1,07 \times 10^3$	$4,98 \times 10^3$	2,47	$6,64 \times 10^3$	2,62
Lt_0*	0,285	$8,07 \times 10^2$	$7,12 \times 10^3$	3,50	$7,80 \times 10^3$	3,11
Pt_0*	0,243	$9,61 \times 10^2$	$5,77 \times 10^3$	2,86	$4,13 \times 10^3$	2,27

The curves obtained in the simulations show that for the same Young's modulus and displacement, the load is higher for the Lt configuration and lower for the Hr configuration. From the experimental curves for the honeycombs of this material, it was possible to verify that the samples Hr_0* and Lt_0* have walls with an E near the lower limit of the manufacturer (38GPa), while the Pt_0* has an E slightly lower than this value ($\sim$ 30GPa).

Numerically, among the aluminum-A honeycombs analyzed, the Lt_0 * model has the highest stiffness and absorbs the most energy, while the Hr_0 * model has the lowest stiffness and the least energy absorbed. It is also noted that for a given value of E, higher stiffness and absorbed energy leads to lower strength of the parts and a more load necessary to produce a given deflection.

Comparing the numerical results with the experimental ones, it is observed that the Hr_0* structure is the one with the lowest value of K and E_a, although in the 3PB tests it is the Pt_0*. However, the order of magnitude of properties K and E_a is identical in both numerical and experimental results.

Figure 6 shows the force-displacement curves obtained in the simulations and experimentally for aluminum-S honeycombs. From these curves, it is noted that, for the same displacement, structures with 0º orientation are those that support the highest load, while the lowest load is supported by structures with 45º orientation.

Figure 7 shows the distribution of von Mises stress obtained in the simulations for aluminum-S structures when Δ = 1.5mm. Table 3 shows the numerical and experimental results of K and E_a obtained from the displacement force curves of these honeycombs and also the maximum von Mises stress.

From the results of table 3, both numerical and experimental, it can be noted that for the same orientation, Lt structures have greater stiffness and absorb more energy than Pt structures, although they have lower strength. The numerical and experimental values of K and E_a grow with orientation in the order 45º, 90º, 0º. Numerically, structures with 90° orientation have the highest strength, while the Lt_0 and

Pt_45 structures have the lowest strength, although the structures in an intermediate situation have $\bar{\sigma}_{max}$ values close to the lowest.

a)

b)

c)
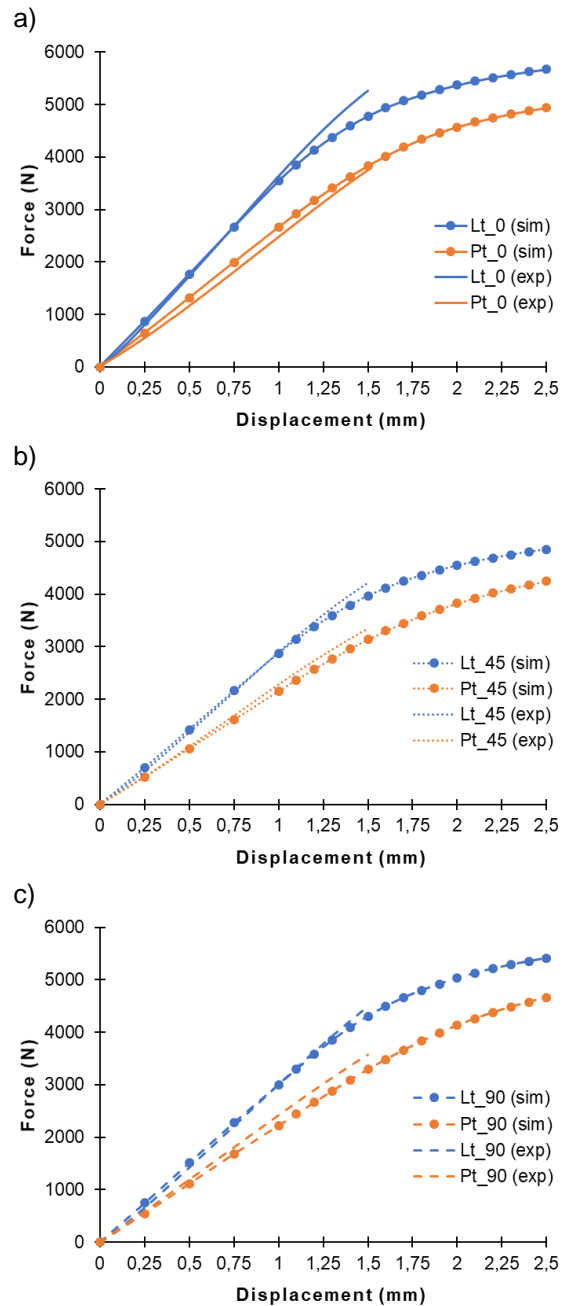
Figure 6: Numerical and experimental force-displacement curves for aluminum-S honeycombs. Models with orientation (a) 0º, (b) 45º, (c) 90º.

5
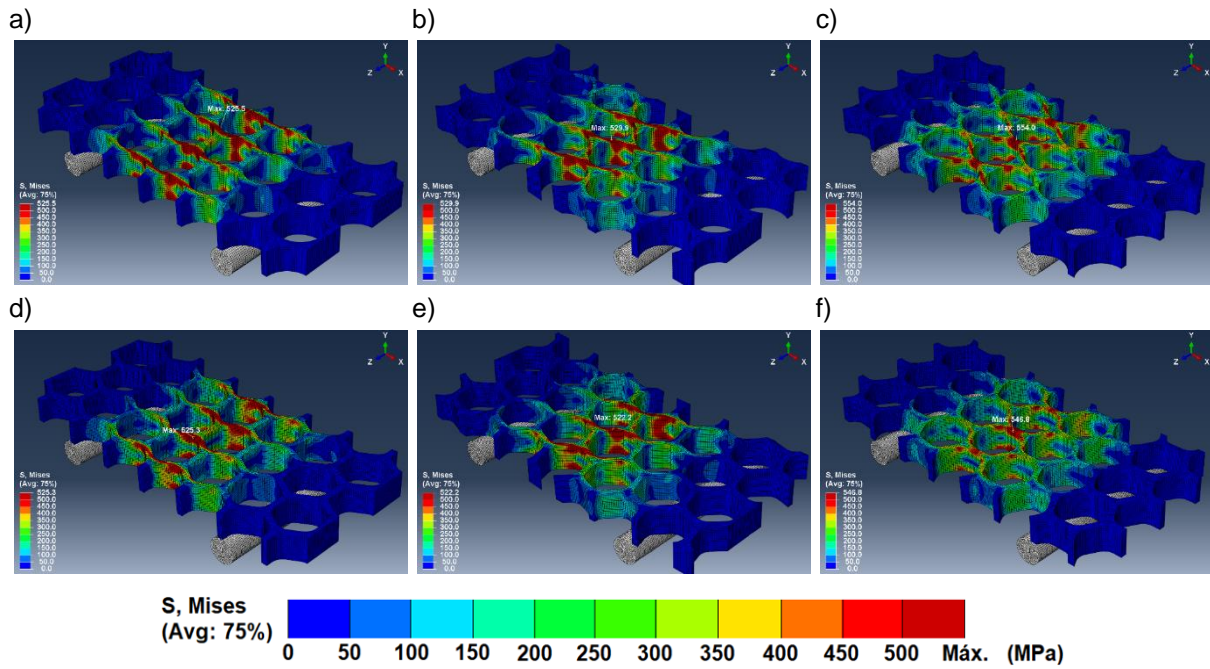
Figure 7: Von Mises stress distribution, when Δ = 1,5mm, for aluminum-S honeycombs. (a) Lt_0, (b) Lt_45, (c) Lt_90, (d) Pt_0, (e) Pt_45, (f) Pt_90.

Table 3: Numerical-experimental properties of aluminum-S honeycombs for Δ = 1,5mm.

Model	$\bar{\rho}$	Finite elements			Experimental	
		$\bar{\sigma}_{max}/\bar{\rho}$ (MPa)	$K/\bar{\rho}$ (N/mm)	$E_a/\bar{\rho}$ (J)	$K/\bar{\rho}$ (N/mm)	$E_a/\bar{\rho}$ (J)
Lt_0	0,285	$1,85 \times 10^3$	$1,25 \times 10^4$	13,6	$1,33 \times 10^4$	14,1
Lt_45	0,286	$1,86 \times 10^3$	$1,01 \times 10^4$	11,1	$1,07 \times 10^4$	11,2
Lt_90	0,284	$1,95 \times 10^3$	$1,07 \times 10^4$	11,8	$1,12 \times 10^4$	11,7
Pt_0	0,243	$2,16 \times 10^3$	$1,10 \times 10^4$	12,2	$1,10 \times 10^4$	11,3
Pt_45	0,244	$2,14 \times 10^3$	$8,85 \times 10^3$	9,8	$9,73 \times 10^3$	9,3
Pt_90	0,242	$2,26 \times 10^3$	$9,16 \times 10^3$	10,3	$1,01 \times 10^4$	11,2

From the results presented in tables 2 and 3 for the stiffness and energy absorbed by the aluminum structures, it is clear that there is a good agreement between simulations and experimental tests. For aluminum-A models, this agreement was reached while assuming the material was isotropic. Effectively, when producing parts using SLM technology, a specific crystallization direction is not achieved. Therefore, anisotropy hardly exists. For aluminum-S models, because honeycombs have been machined from an isotropic plate, the walls of the structures are very close to isotropy as well.

Figure 8 shows the force-displacement curves obtained from simulations and experimental tests for PLA honeycombs. According to the numerical curves, for a given configuration and the same displacement, structures with 0º orientation are the ones with higher load, while the lowest load is supported by structures with 45º orientation. On the other hand, for the same orientation, the highest load is supported by the Lt structures and the lowest load by the Hr structures. Comparing the numerical with the experimental curves, a discrepancy in the load values for a given displacement is evident. However, qualitatively the trends described above to numerical curves remain for experimental behavior.

Table 4 presents the numerical and experimental results of K and E_a for PLA honeycombs and also the maximum von Mises stress when Δ = 2.5mm. For the same configuration, structures with 0º orientation have the highest stiffness, while structures with 45º orientation have the lowest stiffness. This trend is observed by both numerical and experimental results, although simulation results underestimate all experimental K values. However, the order of magnitude of the values is predicted correctly.

Numerically, the values of E_a as a function of the orientation of the structures show the same
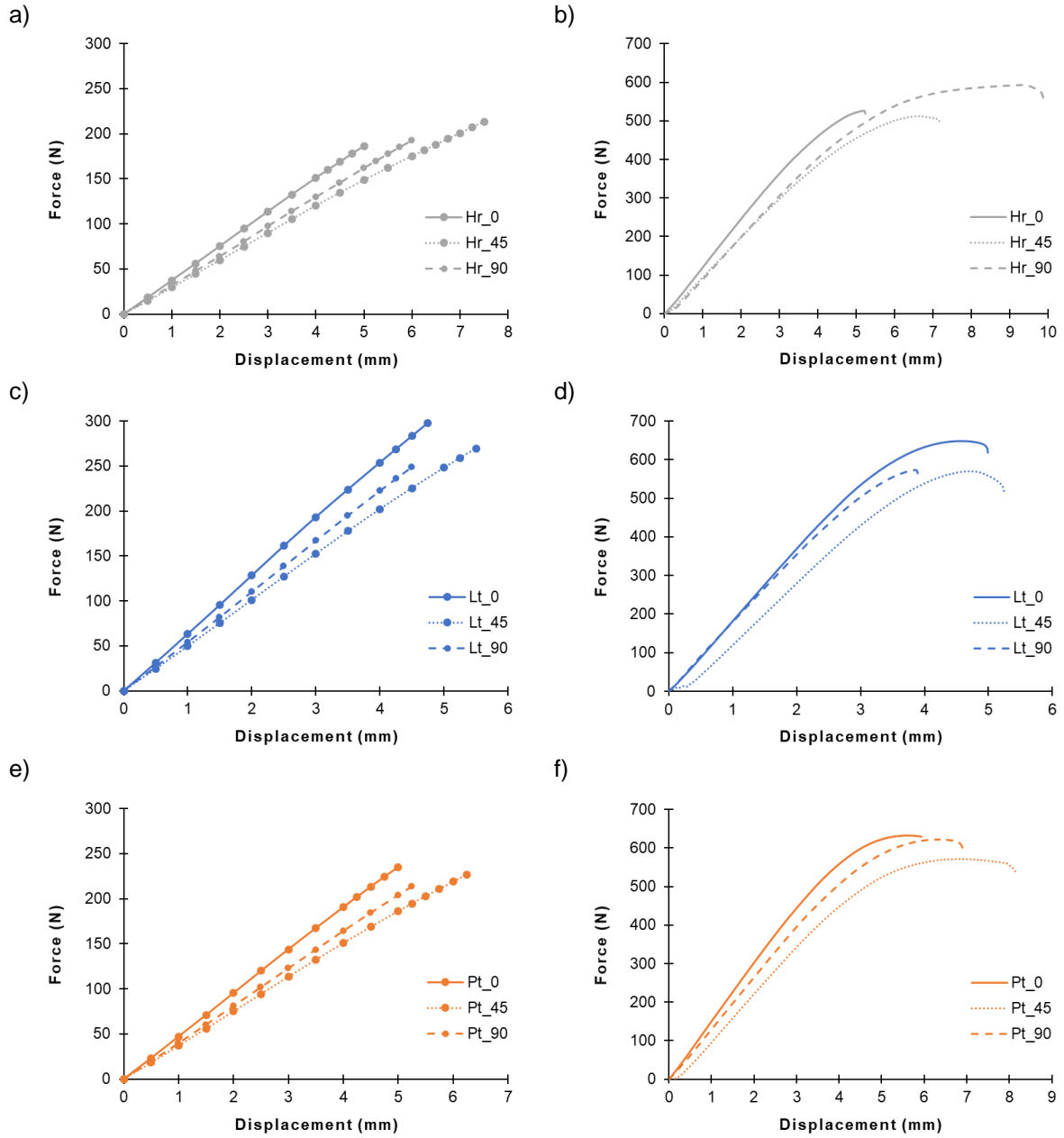
Figure 8: Force-displacement curves for PLA honeycombs up to Δ at fracture. (a), (c), (e) Numerical curves. (b), (d), (f) Experimental curves. Configuration: (a) - (b) Hr, (c) - (d) Lt, (e) - (f) Pt.

Table 4: Numerical-experimental properties of PLA honeycombs for Δ = 2,5mm.

Model	$\bar{\rho}$	Finite elements			Experimental	
		$\bar{\sigma}_{max}/\bar{\rho}$ (MPa)	$K/\bar{\rho}$ (N/mm)	$E_a/\bar{\rho}$ (J)	$K/\bar{\rho}$ (N/mm)	$E_a/\bar{\rho}$ (J)
Hr_0	0,223	$1,35 \times 10^2$	$1,70 \times 10^2$	0,526	$5,64 \times 10^2$	1,70
Hr_45	0,224	$9,77 \times 10^1$	$1,35 \times 10^2$	0,414	$4,66 \times 10^2$	1,34
Hr_90	0,222	$1,31 \times 10^2$	$1,45 \times 10^2$	0,448	$4,94 \times 10^2$	1,32
Lt_0	0,285	$1,11 \times 10^2$	$2,24 \times 10^2$	0,701	$6,60 \times 10^2$	2,01
Lt_45	0,286	$9,82 \times 10^1$	$1,79 \times 10^2$	0,550	$5,61 \times 10^2$	1,43
Lt_90	0,284	$1,19 \times 10^2$	$1,97 \times 10^2$	0,602	$6,22 \times 10^2$	1,96
Pt_0	0,243	$1,27 \times 10^2$	$1,98 \times 10^2$	0,612	$6,28 \times 10^2$	1,94
Pt_45	0,244	$1,02 \times 10^2$	$1,56 \times 10^2$	0,478	$5,18 \times 10^2$	1,33
Pt_90	0,242	$1,27 \times 10^2$	$1,70 \times 10^2$	0,520	$5,56 \times 10^2$	1,69

7

evolution as the stiffness values. The same happens with the experimental values of E_a, except for the Hr configuration, where the structure Hr_90 is the least energy absorbed instead of the structure Hr_45. Like stiffness, E_a values for PLA honeycombs continue to be underestimated compared to experimental ones. Further, in this case, the order of magnitude is also underestimated, unlike stiffness.

Nevertheless, a large difference between the numerical and experimental values of stiffness and absorbed energy was found for PLA honeycombs, unlike for metallic structures. These two parameters were underestimated in the simulations as a result of using FDM technology in the production of samples and assuming in the modeling that the material was isotropic. It should be noted that the tensile test specimens from which Young's modulus was determined are mainly formed by infill. Since infill has lower stiffness and strength than shells, the E value used in modeling is lower than the honeycomb walls, where shells make up much of the structure rather than infill. The

fact that the numerical values of K and E_a, on average, are closer to the experimental values for Lt configuration honeycombs, followed by Pt and finally Hr, corroborates this explanation, since it is in this order (Lt, Pt, Hr) that the percentage by volume of infill in a sample decreases.

Analyzing the values of $\bar{\sigma}_{max}$, for the same configuration, the structures with 45⁰ orientation have the lowest strength. On the other hand, the structures with higher strength have both 0⁰ and 90⁰ orientations, namely, correspond to the structures Hr_0, Lt_90, Pt_0, and Pt_90. For structures with 0° and 90° orientations, the Lt configuration has the lowest strength, while the Hr configuration has the highest. The exception to the aforementioned trend is in 45° orientation structures, where the Hr configuration has the least strength and the Pt configuration the largest. Figure 9 shows the distribution of the plastic strain magnitude (PEMAG variable) in PLA honeycombs, for the Δ where the fracture is expected to occur. Figure 10 shows the PLA samples after 3PB tests.
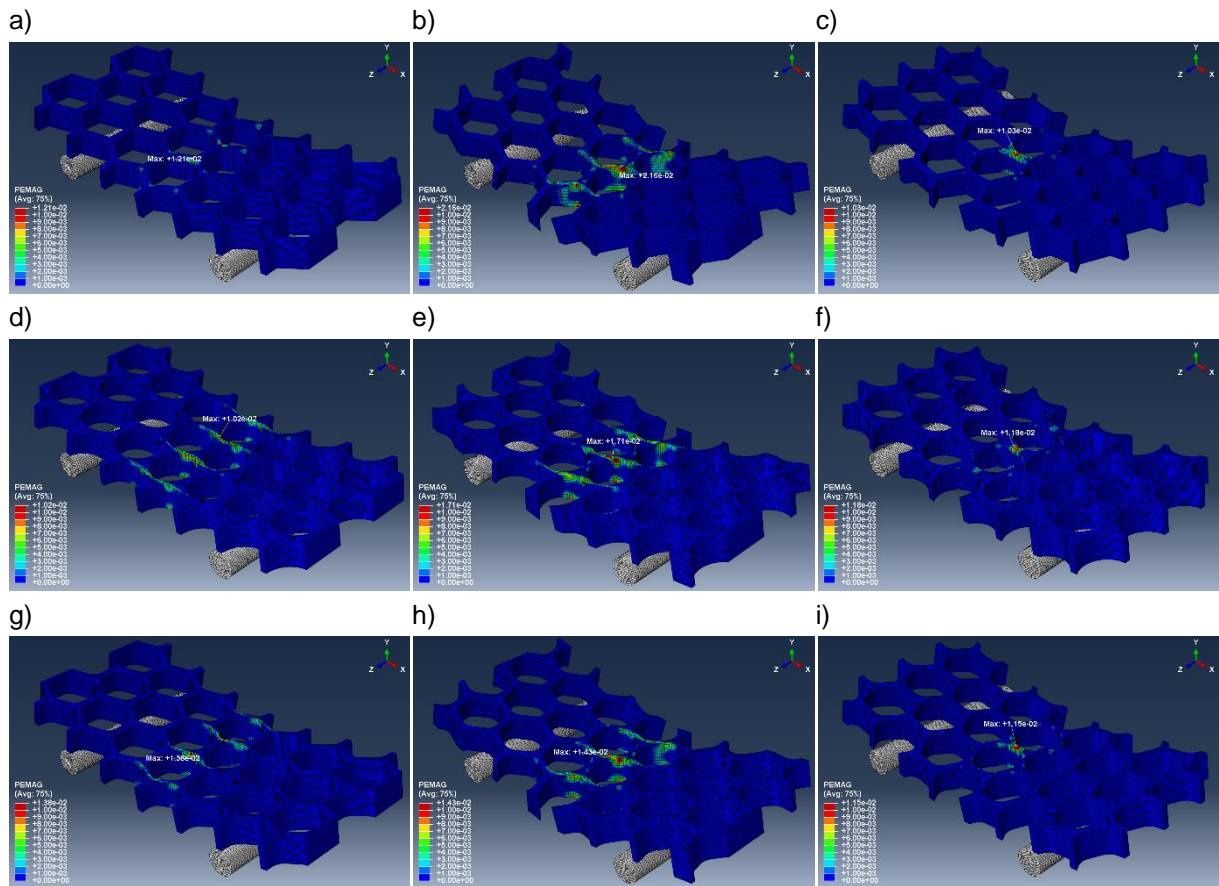
Figure 9: Distribution of PEMAG variable at Δ where PLA honeycomb fracture is predicted (zones in red are where plastic strain magnitude is greatest). (a) Hr_0, (b) Hr_45, (c) Hr_90, (d) Lt_0, (e) Lt_45, (f) Lt_90, (g) Pt_0, (h) Pt_0, (i) Pt_0.

Starting by analyzing the Hr structures with the 0° and 45° orientations, it appears that the fracture begins at the triple junctions, which correspond to stress concentrating zones. However, the Hr_90 structure has a high deformation and there is also fracture in the structs at the center of the honeycomb. Fracture of Lt structures occurs in areas of the walls of the honeycomb with the smaller resistant area, away from the unit cell vertices. Finally, for Pt structures, the failure mode is different for each orientation. In structures Pt_0 and Pt_45, the fracture begins at the Plateau borders, in zones where the resistant area is smaller. On the other hand, in the Pt_90 structure, the failure mode is similar to that of the Hr_90 structure, since the fracture begins midway through the structs. It is thus noted that the failure mode of the Pt structures is identical to that of the Hr structures, although the triple junctions in the Pt configuration are reinforced. When comparing the fracture of the samples with the results obtained in the simulations for the PEMAG variable, it is clear that, globally, the fracture starts in the zones where the simulations predict the greatest plastic strain, ie, where the PEMAG is maximum or high.

It is also noted that in all structures analyzed the fracture occurs in the central section of honeycombs. However, the EF results predict fracture at the top of PLA honeycombs, whereas experimentally it occurs at the bottom. One explanation for this is that the contact interaction used in numerical modeling leads to higher stresses within the contact area than the actual ones due to the numerical formulation used by the software. In fact, for von Mises stress distribution for aluminum-S honeycombs (figure 7) the same is true. Experimentally, like what happens in a solid and homogeneous material in pure bending, the fracture of PLA honeycombs occurs in the bottom, due to traction.
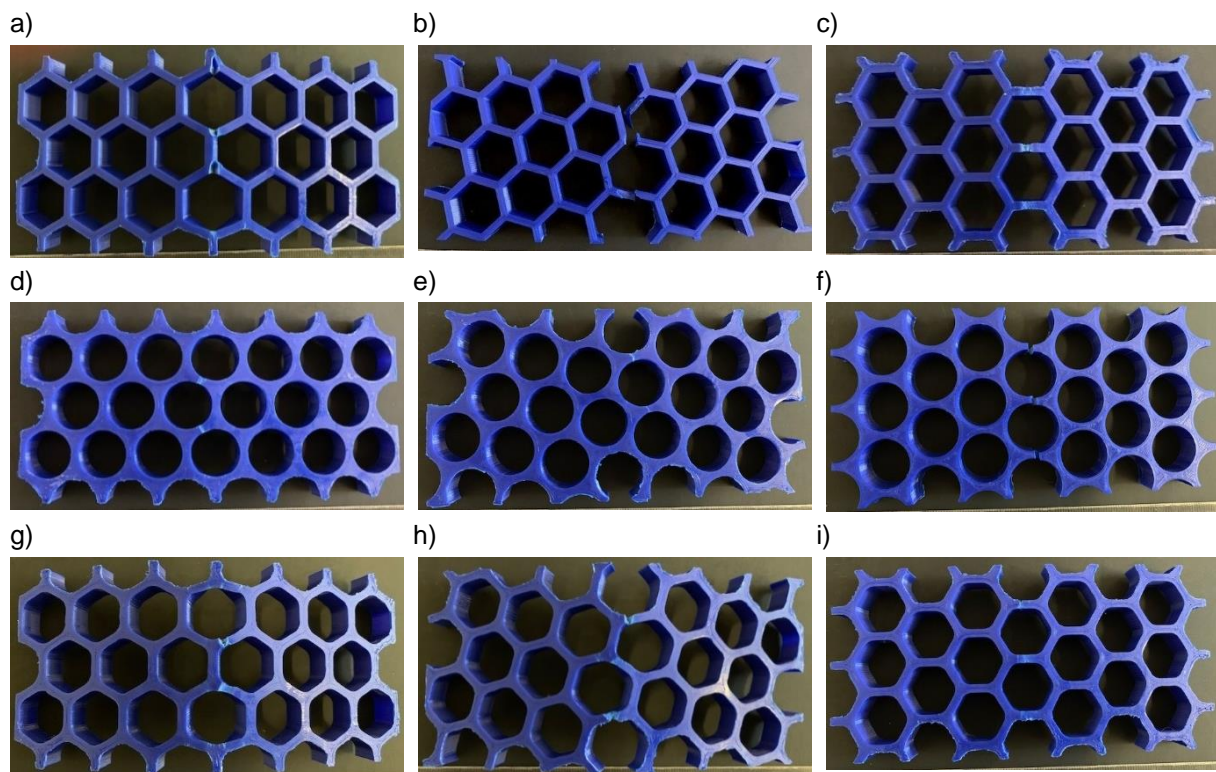
Figure 10: PLA samples after 3PB tests. (a) Hr_0, (b) Hr_45, (c) Hr_90, (d) Lt_0, (e) Lt_45, (f) Lt_90, (g) Pt_0, (h) Pt_0, (i) Pt_0.

4. **Conclusions**

In this work, three configurations and orientations in the plane for honeycomb structures were studied. The drawn structures were numerically simulated and experimentally tested in 3-point bending tests. The fracture of the PLA structures was also analyzed with the PEMAG variable (plastic strain magnitude), which was compared with the sample photos after the tests.

A von Mises stress convergence analysis showed that to have an error of less than 2% it is necessary to mesh Hr and Pt structures with a global size equal to 0.6mm, while 0.7mm for Lt structures.

Overall, a very good correlation between numerical and experimental results was found.

Among the three orientations analyzed, either from numerical or experimental results, the structures with 0º orientation are those that have the highest stiffness and the most energy absorbed. Also, in general, for the same configuration, 45 ° orientation structures have the lowest stiffness and the lowest energy absorbed.

On the other hand, for the same orientation, Lt structures have higher stiffness and absorb more energy than Pt structures. In this study, it was also found that, in general, Hr structures have lower stiffness and absorb less energy than Pt structures.

Regarding the strength of structures, the results show a strong sensitivity with the geometry (configuration and orientation) as well as with the type of material.

As regards the fracture of PLA honeycombs, for Hr structures it is located at the triple junctions (stress concentration zones) in general. In Lt structures, the fracture occurs in the wall zones of smaller resistant areas. Finally, usually, Pt structures fracture around Plateau borders where the resistant area decreases. Also, there is no relationship between honeycomb fracture and orientation, unlike configuration.

In conclusion, since the Lt structures with 0º orientation have the highest stiffness and absorb the most energy within the analyzed cases, they are alternatives to traditional honeycombs in applications where these two properties are required.

References

[1] L. J. Gibson and M. F. Ashby, *Cellular solids: Structure and properties, Second edition*. Cambridge University Press, 1997.

[2] T. Bitzer, *Honeycomb Technology: Materials, Design, Manufacturing, Applications and Testing*. 1997.

[3] I. Carranza *et al.*, "Characterising and modelling the mechanical behaviour of polymeric foams under complex loading," *J. Mater. Sci.*, vol. 54, no. 16, pp. 11328–11344, 2019.

[4] D. Pollard, C. Ward, G. Herrmann, and J. Etches, "The manufacture of honeycomb cores using Fused Deposition Modeling," *Adv. Manuf. Polym. Compos. Sci.*, vol. 3, no. 1, pp. 21–31, 2017.

[5] E. E. Gdoutos, I. M. Daniel, K. A. Wang, and J. L. Abot, "Nonlinear behavior of composite sandwich beams in three-point bending," *Exp. Mech.*, vol. 41, no. 2, pp. 182–189, 2001.

[6] Y. Du, H. Li, Z. Luo, and Q. Tian, "Topological design optimization of lattice structures to maximize shear stiffness," *Adv. Eng. Softw.*, vol. 112, pp. 211–221, 2017.

[7] L. Yang *et al.*, *Additive Manufacturing of Metals: The Technology, Materials, Design and Production*, 1st ed. Springer International Publishing AG, 2017.

[8] A. Y. Hussein, "The Development of Lightweight Cellular Structures for Metal Additive Manufacturing," University of Exeter, 2013.

[9] A. H. Azman, "Method for integration of lattice structures in design for additive manufacturing," Université Grenoble Alpes, 2018.

[10] C. Zhu *et al.*, "Nano Today 3D printed functional nanomaterials for electrochemical energy storage," *Nano Today*, vol. 15, pp. 107–120, 2017.

[11] "Introduction to FDM 3D printing | 3D Hubs." [Online]. Available: https://www.3dhubs.com/knowledge-base/introduction-fdm-3d-printing. [Accessed: 24-Sep-2019].

[12] 3D Hubs, "Selecting the optimal shell and infill parameters for FDM 3D Printing." [Online]. Available: https://www.3dhubs.com/knowledge-base/selecting-optimal-shell-and-infill-parameters-fdm-3d-printing. [Accessed: 02-Aug-2019].

[13] W. Ronan, V. S. Deshpande, and N. A. Fleck, "The tensile ductility of cellular Solids: The role of imperfections," *Int. J. Solids Struct.*, vol. 102–103, pp. 200–213, 2016.

[14] C. M. S. Vicente, J. Fernandes, L. Reis, A. M. De Deus, M. F. Vaz, and M. Leite, "Effect of protective coatings on the water absorption and mechanical properties of 3D printed PLA," *Frat. ed Integrita Strutt.*, vol. 13, no. 48, pp. 748–756, 2019.

[15] SLM Solutions, "Material Data Sheet - Al-Alloy AlSi7Mg0,6 / EN AC-42200." .

[16] thyssenkrupp, "Aluminum Stock Guide." .

[17] S. Farah, D. G. Anderson, and R. Langer, "Physical and mechanical properties of PLA, and their functions in widespread applications — A comprehensive review," *Adv. Drug Deliv. Rev.*, vol. 107, pp. 367–392, 2016.